

Busting the Paper Ballot: Voting Meets Adversarial Machine Learning

Kaleel Mahmood
University of Rhode Island
Department of Computer Science and
Statistics
Kingston, Rhode Island, United States
kaleel.mahmood@uri.edu

Caleb Manicke
University of Connecticut
Voting Technology Center
Storrs, Connecticut, United States
caleb.manicke@uconn.edu

Ethan Rathbun
Northeastern University
Khoury College of Computer Sciences
Boston, Massachusetts, United States
rathbun.e@northeastern.edu

Aayushi Verma
University of Connecticut
Voting Technology Center
Storrs, Connecticut, United States
aayushi.verma@uconn.edu

Sohaib Ahmad
University of Connecticut
Voting Technology Center
Storrs, Connecticut, United States
sohaib.ahmad@uconn.edu

Nicholas Stamatakis
Stony Brook University
Department of Computer Science
Stony Brook, New York, United States
nikola268345@gmail.com

Laurent Michel
Synchrony Chair in Cybersecurity
University of Connecticut
Voting Technology Center
Storrs, Connecticut, United States
laurent.michel@uconn.edu

Benjamin Fuller
University of Connecticut
Voting Technology Center
Storrs, Connecticut, United States
benjamin.fuller@uconn.edu

ABSTRACT

We show the security risk associated with using machine learning classifiers in United States election tabulators. The central classification task in election tabulation is deciding whether a *mark* does or does not appear on a *bubble* associated to an alternative in a contest on the ballot. Barretto et al. (E-Vote-ID 2021) reported that convolutional neural networks are a viable option in this field, as they outperform simple feature-based classifiers.

Our contributions to election security can be divided into four parts. To demonstrate and analyze the hypothetical vulnerability of machine learning models on election tabulators, we first introduce four new ballot datasets. Second, we train and test a variety of different models on our new datasets. These models include support vector machines, convolutional neural networks (a basic CNN, VGG and ResNet), and vision transformers (Twins and CaiT). Third, using our new datasets and trained models, we demonstrate that traditional white box attacks are ineffective in the voting domain due to gradient masking. Our analyses further reveal that gradient masking is a product of numerical instability. We use a modified difference of logits ratio loss to overcome this issue (Croce and Hein, ICML 2020). Fourth, in the physical world, we conduct attacks with the adversarial examples generated using our new methods. In traditional adversarial machine learning, a high (50% or greater) attack success rate is ideal. However, for certain elections, even a 5% attack success rate can flip the outcome of a race. We show such an

impact is possible in the physical domain. We thoroughly discuss attack realism, and the challenges and practicality associated with printing and scanning ballot adversarial examples.

KEYWORDS

Election Security, Adversarial Machine Learning

ACM Reference Format:

Kaleel Mahmood, Caleb Manicke, Ethan Rathbun, Aayushi Verma, Sohaib Ahmad, Nicholas Stamatakis, Laurent Michel, and Benjamin Fuller. 2025. Busting the Paper Ballot: Voting Meets Adversarial Machine Learning. In *Proceedings of the 2025 ACM SIGSAC Conference on Computer and Communications Security (CCS '25)*, October 13–17, 2025, Taipei, Taiwan. ACM, New York, NY, USA, 17 pages. <https://doi.org/10.1145/3719027.3744882>

1 INTRODUCTION

Elections in the United States are decentralized and conducted by the states. The Help America Vote Act of 2002 prompted all states to modernize their voting infrastructure and retire lever machines. States overwhelmingly adopted voter marked paper ballots that yield a “voter verifiable paper audit trail” or VVPAT [1] and are scanned and counted by digital tabulators. According to Verified Voting Database, 69.2% of tabulators are scanners and 25.9% are ballot marking devices (BMD), leaving only a 4.9% market share for direct recording devices that do not use paper at all.¹ To assess the voter selection for any contest on a ballot, the tabulator determines whether *bubbles* associated to alternatives in the contest are *blank* or *marked*. Namely, the core task is to carry out a binary classification on the digital image of a bubble. Barretto et al. argued that

¹We exclude ballot marking devices that print two versions of the voter’s preferences: one readable by the voter and a machine interpretation such as a QR code that is ingested by the tabulation.

CCS '25, October 13–17, 2025, Taipei, Taiwan.

© 2025 Copyright held by the owner/author(s).

This is the author’s version of the work. It is posted here for your personal use. Not for redistribution. The definitive Version of Record was published in *Proceedings of the 2025 ACM SIGSAC Conference on Computer and Communications Security (CCS '25)*, October 13–17, 2025, Taipei, Taiwan, <https://doi.org/10.1145/3719027.3744882>.

Convolutional Neural Networks (CNNs) [2] are suitable for ballot mark recognition with up to 99.9% accuracy on manually labeled ballots. However, machine learning classifiers are vulnerable to adversarial examples [3] where an imperceptible perturbation added to the input induces a misclassification.

This paper explores the susceptibility of machine learning classifiers to adversarial attacks when presented with images of bubbles from the voting domain. Specifically, our paper introduces attacks where one can implant adversarial machine learning examples [3–5] on ballots handled by the voter before it is fed to the tabulator. An adversarial signal is visually imperceptible (to a human), yet alters the classification results. *We focus on attacks that could be conducted by a compromised vendor that prints ballots.* The attacker’s goal is to print a ballot that appears empty but where some bubbles are interpreted as marked by the tabulator. We detail our threat model in Section 4. This voting domain is unique for the following reasons:

- (1) It focuses on a deceptively simple binary classification.
- (2) Voluntary voting system guidelines (VVSG) 2.0 require publication by vendors of the mechanisms used to classify a bubble,² making *white box attacks* realistic.
- (3) The attacker has to print a *signal* on paper which is scanned. Effects such as printer dithering must be considered. Kurakin et al. [6] previously considered attacks in the physical world. Our physical world setting differs from prior work.
- (4) There are no agreed-upon labeled datasets for mark classification. Human auditors are expected to capture voter intent with guidelines that vary by state (see discussion in Section 3.1).
- (5) An attacker can freely reuse adversarial examples; bubbles printed on a ballot are supposed to be identical.
- (6) Election equipment has a long life cycle. Deploying vulnerable models carries lasting risks.

We conduct our attacks on six representative models, a support vector machine (SVM), a three-layer CNN that we call SimpleCNN, VGG-16 CNN [7], a ResNet-20 CNN [8], Class Attention in Image Transformer (CaiT) [9], and the Twins vision transformer [10].

Our Contribution. We demonstrate the hypothetical vulnerability of using machine learning classifiers in bubble recognition in both the digital and physical setting. In doing so we make the following contributions:

- (1) **New Labeled Voting Datasets:** We introduce four new labeled ballot datasets (two grayscale and two color) for training machine learning classifiers for ballot mark recognition [11].
- (2) **Gradient Masking on Voting Datasets:** We show that for the three convolutional models, the conventional application of white-box attacks (APGD [12], PGD [13] and MIM [14]) does not work. Models show robustness > 0 when the adversary can apply unbounded perturbations. This failure is attributed to numerical instability causing gradients in back-propagation to be reported as 0, despite the models achieving high accuracy during training. To the best of our knowledge, all previous examples of gradient masking occurred via defensive methods to stop adversarial examples [15].

- (3) **Overcoming Gradient Masking:** We modify the difference of logits ratio (DLR) proposed by Croce and Hein [12] to work for binary classification (our modification can be viewed as an untargeted version of Carlini and Wagner’s loss [16]).
- (4) **Physical Attacks:** We show that the printing and scanning process (using commodity equipment) drastically degrades the adversarial attack signal. Despite this, some attacks on some models are effective enough to still impact election races with small margins where many voters do not specify a preference.

Disclaimer. We intentionally target common classification models rather than any model used by a tabulator. No tabulator manufacturers has been certified to VVSG 2.0, so details are not yet available on their classification methods. The purpose of this work is to highlight the risk in potentially deploying machine learning models in these systems. As discussed in Appendix C on ethical considerations, our target machine learning models are chosen to cover the design space. They are not an attempt to recreate choices made by vendors. Ballot printers are specialized vendors with long-term relationships with municipalities. We believe an external attack on a vendor is more likely than an insider intentionally compromising ballot printing.

Paper Organization. Section 2 details election systems in the United States. Section 3 present the new datasets and classifiers under test. Section 4 describes our adversarial threat model and adversarial example generation methods. Section 5 shows that gradient masking occurs on our datasets after standard training. Section 6 how DLR overcomes gradient masking. Section 7 presents our experimental results and analyses in the digital domain. Section 8 details our physical domain attack results. Section 9 concludes and presents open questions. Our Appendix contains further experimental details. Classifiers under test and attacks are at <https://github.com/VoterCenter/Busting-the-Ballot>.

2 VOTING IN THE UNITED STATES AND PRIOR WORK

This section provides an overview of voting practices and related security research in the United States. Voting processes are meant to enforce the 1-voter to 1-vote principle to assure fairness. Voting by mail and voting in person rely on different processes suitable to each modality. This work focuses on in-person voting. This process involves multiple steps 1) checking-in voters, 2) handing out ballots, 3) voting and casting of a ballot and 4) tabulating the results. This paper further restricts its scope to the latter steps of this pipeline: voting, casting and tabulating. Voting systems used in the U.S. include:³⁴

Ballot Scanners. Take in ballots with bubbles and determine which bubbles on the ballot have been filled in. The appeal of scanners (used in 66.6% of the U.S.) is that ballots are typically marked directly by voters and form a VVPAT. The VVPAT can be used for machine independent audits.

²Requirement 1.1.6G and accompanying discussion.

³See an overview at Verified Voting. Observe that smaller categories exist, including DREs, that create voter-verifiable paper trails.

⁴Eliding research on Internet [17] and cryptographic [18–20] voting.

Ballot Marking Devices. Provide the necessary means to *fill* bubbles on behalf of the voter based on an alternate (often digital and computerized) input mechanism instead of a pen. A voter using a BMD fills in a digital artifact, that creates a printout of a filled ballot. Some BMDs fill in bubbles and rely on conventional paper ballots. Others encode the ballot in a machine readable format (like a QR code, or a barcode) or print the selection in each race as plain text.⁵ Selections, conveyed through filled bubbles, are interpreted primarily by a tabulator as in the previous method. Precincts with BMDs account for 25.9% of the U.S. electorate.

Direct Recording Equipment. Voters use an interface to state their preferences and the machine records these preferences and adds them to a tabulation. The DRE device is used for all 3 stages: encoding a ballot, casting the ballot and tabulating all the ballots. There is no paper artifact of the voter's preferences. These systems are used in roughly 4% of the U.S.⁶ Our work does not apply to DREs, but these systems are shunned due to the lack of a VVPAT [21].

2.1 Types of Ballot Scanners

Ballot scanners are given a page containing several *questions*, each with multiple outcomes that can be chosen by filling a bubble. The scanner classifies each bubble as a blank or a marked bubble. These determinations are then used with election-specific rules to determine the votes.

Optical Lens Systems. This analog technology is ubiquitous in standardized tests where examinees fill bubble sheets that convey answers. Each page features *timing marks* (black rectangles) on its edges to hint at the position of logical rows and columns. All the bubbles on the page form a matrix and are addressable based on their row and column indices. Scanners process one row at a time (when facing a row timing mark), effectively opening an analog sensor to collect reflected light. The machine has a light sensor in each column position. If a bubble is filled, it absorbs more light than a blank bubble. Whether bubbles are read as marked depends on the thresholds and sensitivity of the sensors. Image segmentation is a function of timing marks and sensor position.

Full Image Scanners. Off-the-shelves full-image scanners are also used. Modern hardware can record anything from 100 dots-per-inch to 1200 dots-per-inch. Given a 8x11 US letter page, a 200 DPI resolution implies that each row has $1700 = 8.5 \cdot 200$ pixels and a grand total of $2200 = 11 \cdot 200$ rows. Sensors typically captures several rows at a time and the pixels are physically arranged in a so called *Bayer* pattern. The firmware of the scanner (or the driver on the host computer) converts the Bayer matrix of grayscale values into a matrix of RGB values by reconstructing the missing color values through interpolation. This process is known as debayering or demosaicing [22]. The end result is a RGB pixels where each color channel is grayscale and uses 8 bits per pixel. Pulling the page over the sensor is a mechanical process subject to acceleration and deceleration. The sensor sensitivity impacts the color rendition of the device. Once acquired by a COTS Scanner, an image is analyzed using the following steps:

- *Stretching* The raw image has an effective DPI rate that varies with the acceleration of the ballot. A correction *inverts* this stretch to bring features closer to their true relative location.
- *Registration* A constellation of geometric features identified on a reference ballot are used to align any incoming scan with the reference image. Once this is done, a bubble at coordinate (x, y) in the reference image is expected to be at coordinate (x, y) in the registered scan.
- *Chromatic Correction* An ICC profile corrects the colors in the image to bring them as close as possible to the true colors based on a device specific colorimetry calibration.
- *Segmentation* The location of the bubbles on the reference image is used to locate and clip out small RGB bitmaps that contain the actual bubbles.
- *Classification* The final step classifies each bitmap as a blank bubble or a marked bubble.

Once bubbles are classified as blanks or marks, each race on the ballot can be tabulated according to the rules of the race. The ultimate tabulation stage is not the object of this paper. We also assume that all stages up to and including segmentation are accurate.

Prior Work. Tabulation security received renewed attention [23–32] after the Help America Vote Act in 2002. Issues ranged from unprotected serial ports, manipulation of election definitions, and exploitation of poorly designed cryptography. Procedures including risk-limiting audits or RLAs [33–37] were created to deal with these vulnerabilities. Note that RLAs only detect *whether there is an error in the reported outcome*. Detecting the root cause of such errors can be complicated or impossible. Other classes of vulnerabilities include lax adherence to policy [38]. Procedures and requirements are formalized in voluntary voting system guidelines or VVSG [39–41].

Vulnerabilities persists in modern systems [42] including the fact that voters do not always inspect the output of BMDs [43, 44]. Imprinting of identifiers on ballots at tabulation time, which enables more efficient RLAs (see discussion in [36]), also requires careful use of cryptography [45]. These vulnerabilities have rightly placed the design of secure ballot tabulation devices as a primary focus for the community.

3 DATASETS / CLASSIFIER ARCHITECTURES

This section introduces four new datasets of segmented regions on a ballot for interpretation. These are images of *bubbles*. For each dataset, we define its properties and utility for further investigation. Datasets and the accompanying software are released alongside this paper. The remainder of the section reviews each ML classifiers and explains the purpose for inclusion in the analyses.

3.1 New Bubble Datasets

Images are segmented using ballot geometry. We do not consider image segmentation as an attack target. Mark interpretation is a supervised binary classification problem, requiring representative datasets of marks and empty bubbles [2]. The segmented images are 40×50 pixels. Fully darkened bubbles should be interpreted as marks while empty bubbles should be interpreted as nonmarks. Naturally, one would need some separation oracle to define a boundary between marks and nonmarks. No matter what oracle is chosen,

⁵A recent executive order, Preserving and Protecting the Integrity of American Elections, asks for all preferences to be printed in plain text.

⁶There are variants not reviewed here so the numbers do not add to 100%.

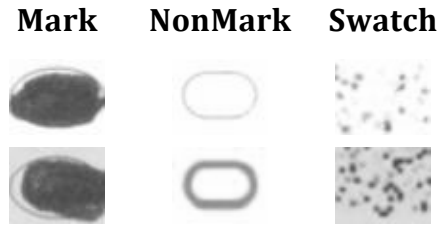


Figure 1: Types of examples in our dataset. The swatches are artificial marks designed to be close to the border between a mark and a non-mark for an optical scan. The darker backgrounds are the result of using colored stock paper.

some images will be very *close* to the boundary. Such images are called *marginal marks* [46] and may include samples such as checkmarks, crosses, lightly filled or even accidentally filled bubbles, see [46, Table 1]. Rules for interpreting marginal marks vary across municipalities. The desire to account for voter intent⁷ complicates the question of what images should be in a training set and how they should be labeled. In all datasets, labels are produced from an optical lens scanner. Finally, images may be captured as grayscale (8 bpp) or color (RGB, 24 bpp) artifacts. We present four datasets.

Gray-B uses 42,679 images (40×50 , 8 bpp) with blank (35,429 images) and filled (7,250 images) bubbles but no marginal marks. *RGB-B* a 24 bpp color (RGB) version of *Gray-B*.

Gray-C augments *Gray-B* with a collection of marginal marks called “swatches” shown in Figure 1. Swatches are images that vary the position of signal to create samples close to the boundary of an optical lens scanner. The 423,703 randomly generated swatches place equal amounts of random noise throughout each image such that the amount of light is the same. This yields 466,382 labeled images. *RGB-C* is a 24bpp color (RGB) version of *Gray-C*.

Related Voting Datasets. Two other datasets have been used in voting classification research, these are the Humboldt and Pueblo County Datasets. The Humboldt county dataset emerged from Humboldt County Election Transparency Project but it is *not* labeled and we did not have access to a ballot geometry file or a scanner capable of providing labels. Pueblo County allows one to access individual ballot images along with the tabulator interpretation. However, we could not access the entire dataset programmatically.

3.2 Machine Learning Classifiers

This section briefly describes each machine learning model and justifies its inclusion. Details regarding the training and hyper-parameters are given in our anonymous repository.

Support Vector Machine (SVM). SVMs support linear classification [47, 48]. An SVM maximizes the distance between its decision boundary and inputs of each class label in the training set. We used standard linear kernels to represent a simple classifier. Our SVM has 2,001 trainable parameters for *Gray-B* and *Gray-C* and 6,001 trainable parameters for the RGB datasets.

Non-linear kernels such as RBF (Radial Basis Function) could be used to characterize the boundary of non-linearly separable

regions. A non-linear kernel function maps the original data to a higher dimensional space where linear separation may occur [49]. Using kernel functions with SVMs is often done on challenging datasets [50, 51]. Exploring the effectiveness of a non-linear kernel such as RBF is future work.

Why we selected it: The *linear SVM* represents one of the simplest machine learning models that achieves high accuracy on both the *Gray-B* and *RGB-B* datasets. Evaluating the SVM allows us to better understand how robust low-complexity models are to adversarial attacks with voting datasets.

SimpleCNN. Convolutional models are commonly used for image recognition and classification [52]. SimpleCNN is a shallow convolutional neural network that consists of three identical convolutional layers for a total of 28,818 trainable parameters (grayscale) and 29,394 trainable parameters (RGB).

Why we selected it: SimpleCNN bridges the gap in complexity between the *linear SVM* and *deep* convolutional neural networks. Its simple architecture provides a lower-bound accuracy for convolution-based models.

Very Deep Convolutional Network (VGG-16). The VGGNet is a classic convolutional model made to improve AlexNet [53]. The VGGNet architecture restricts the filter size in each convolutional layer to 3×3 . When introduced, VGGNet achieved the largest layer depth when compared to other convolutional models of its time [54]. Our VGG-16 grayscale model has 14,723,010 trainable parameters.

Why we selected it: The VGG is the first “deep” convolution-based neural network. This made the VGG-16 one of the most common benchmarks in traditional image classification [8, 55, 56].

Residual Networks (ResNets). Vanilla deep convolutional neural networks are susceptible to accuracy degradation [57, 58]. Residual Networks (ResNets) [8] offer a solution to this issue. ResNets rely on skip connections between layers. We test a ResNet-20 with 568,033 trainable parameters (grayscale) and 568,321 trainable parameters (RGB).

Why we selected it: ResNets are one of the most widely used types of convolutional neural network. They have been employed in both traditional image classification [59] and in adversarial machine learning extensively [60, 61].

CaiT. Vision transformers are an emerging alternative to convolutional neural networks. Vision transformers benefit from pre-training and their performance excel on image datasets [62]. However, many deep vision transformers suffer from gradient instability and poor feature learning. The Class-Attention in Image Transformers (CaiT) is designed to address these issues in vision transformers [62]. First, a learnable scale parameter is added to regularize residual connections between transformer blocks. Second, CaiT introduces the Class-Attention layer that extracts discriminative features from a class embedding and processed patch embeddings. CaiT has 56,730,626 trainable parameters for our RGB models.

Why we selected it: CaiT is one of the state-of-the-art transformer models that has shown excellent performance on image classification tasks. Therefore, it is a natural choice to use as one transformer based alternative to convolutional neural networks.

⁷Voter Intent Laws Map shows different guidelines, see for example Colorado’s guidelines.

Model (Trained On)	Training Accuracy		Validation Accuracy	
	Bubbles	Combined	Bubbles	Combined
SVM-B	1.0000	.5411	1.0000	.7888
SimpleCNN-B	.9999	.5776	.9999	.7779
VGG-16-B	1.0000	.5351	1.0000	.7859
ResNet-20-B	.9996	.5346	.9998	.7856
Twins-B	1.0000	.5339	1.0000	.7852
CaiT-B	1.0000	.5363	1.0000	.7862
SVM-C	.9473	.7265	.9171	.5953
SimpleCNN-C	1.0000	.9077	1.0000	.9170
VGG-16-C	1.0000	.9224	.9999	.9300
ResNet-20-C	.9997	.9896	.9999	.9087
Twins-C	1.0000	.9194	1.0000	.9357
CaiT-C	.9995	.9069	.9995	.9198

Table 1: Clean training and validation accuracies on bubble and combined datasets for grayscale models.

Twins. The Twins family [10] refines the base vision transformer architecture. We test the Twins-SVT-B architecture. It utilizes locally-grouped self-attention along with globally sub-sampled attention to improve the model’s performance while solely relying on matrix operation to produce predictions. The Twins model trained on grayscale data has 56,067,880 trainable parameters, whereas for RGB it has 56,070,952 parameters.

Why we selected it: Twins is another representative transformer architecture (like CaiT) with excellent performance on vision tasks.

To summarize, we chose six models across a variety of architectures, linear, convolutional, and attention-based, and sizes, from 2K parameters to nearly 57M.

3.3 ML Classifier Performance on Voting Datasets

We focus on the performance of grayscale models. We do not observe meaningful variation of trends or results when training on color models.

All six classifiers were trained on the two gray datasets. Table 1 reports the clean training and validation accuracy for the grayscale models. Two trends are readily apparent. All models, except the SVM trained on *Combined*, achieve a 99% or greater test accuracy on the easy *Gray-B* validation sets, regardless of whether they were trained on *Gray-B* or *Gray-C*. When testing on easy marks, all classifiers are effective, irrespective of their training sets.

Second, high testing accuracy on *Gray-C* (Combined columns) is not achieved by only training on *Gray-B* (-B rows). The testing accuracies are below 80%. Training on *Gray-C* (the -C rows) yields better testing accuracies that range from just 59.6% in grayscale for the SVM to as high as 93.6% for Twins. The SVM model is an exception, performance on *Combined* degrades when trained on combined examples. We hypothesize the SVM is overfitting its linear boundary to the swatch examples which we believe are close to the true “boundary” of the optical scanner.

As mentioned above, an accurate decision boundary for marks other than fully filled bubbles is crucial in real elections. The phenomenon of needing a deep model for high accuracy on complex datasets is consistent with Barretto et al. [2].

4 ADVERSARIAL THREAT MODEL AND ADVERSARIAL EXAMPLE GENERATION

We assume an attacker that compromises ballot printing. The attacker delivers the adversarial examples at the printing stage when blank ballots are either produced, stored in a warehouse, or shipped. The attacker creates printed ballots to be filled out by voters and cast in a tabulator. The attacker has full control of the ballot image and all bubbles must visually *appear* to be empty at the onset. As this “empty” ballot will be inspected and filled by a voter, the goal is to change the classifier output from non-mark to mark while the added signal remains imperceptible.

As we discuss in Section 4.2, one does not need to impact tabulator accuracy much to have an impact, Table 2 shows the number of close state legislative races in battleground states in the 2020 United States Presidential Election with 15% of races having a margin of less than 5%. Our attacks are most harmful when a large number of voters do not specify a preference for the targeted contest. Thus, our attacks are unlikely to impact a presidential race where almost all ballots specify a preference.

4.1 Attack Nomenclature

An attacker that compromises ballot printing can only create examples where a mark appears to be empty but will be classified as a mark. We call this *Over*. For completeness, in the virtual domain we also consider an attacker that perturbs a marked bubble so that it is classified as a nonmark. This is called *Under* as it could lead to a preference being removed and no preference being counted, known as an undervote.

Virtual. First in Section 7, we consider the idealized (for the attacker) *virtual* context where the attacker modifies an image without any intervening printing or scanning. Namely, the adversarial signal cannot be altered (affected) by the steps taken with real physical ballots. We test both *Over* and *Under* in this domain.

Physical. Second in Section 8, the paper considers the more realistic *physical* context where adversarial examples are organized onto sheets of paper which are printed and then scanned using COTS hardware, namely an HP LaserJet-3010 series and a Fujitsu-7600 scanner. The resulting images are registered, color-corrected, and segmented (see an overview in Section 2). Laser printing is a noisy process. Laserjet printers use dithering to cope with fewer than 256 greyscale levels and simulate gray intensities. Commercial offset printing yields less noise. Yet, tabulators must handle images from commodity printers (such as on-demand ballot printers) as municipalities print ballots when they run out. In this domain we only test *Over* examples. In the stringent and realistic physical settings where the adversarial signal is printed on paper it is possible to cause misclassification of non-marks to marks at a high enough rate to impact close elections. This work offers evidence that tabulators using machine learning algorithms are susceptible to adversarial attacks that cause empty bubbles to be interpreted as marks.

4.2 Analyzing Attacks on Voting Systems

Attacking voting systems is distinct from conventional adversarial machine learning in two facets. First, a high attack success rate is not required to impact an election. Second, when a misclassification

2020	Races	5%	2%	1%	Blank %
Arizona	90	16	6	4	-
Nevada	52	12	3	2	11.7%
Georgia	236	14	5	2	8.9%
North Carolina	170	15	4	0	4.7%
Pennsylvania	228	12	3	1	7.0%

Table 2: Number of tight state legislative races in United States Battleground States in 2020 Presidential Election. We omit Arizona as each district elects two legislators and many of these districts have at most 2 candidates.

does occur, several different actions can be taken by the voting system. We detail differences in this subsection. When the classifier perceives a *Over* example one of three things occurs:

- (1) If the voter did not fill any bubbles in that race (e.g. a local race in a presidential election), the attacker has created a vote for a candidate in that race. The Leon County Post Election Audit of 2022 found that 19% of voters leave at least one race blank. In the 2020 Presidential Election in Nevada (a battleground state), 12% of voters did not vote for their state legislative race.
- (2) If the voter marks the same preference as the adversarial bubble, the choice is aligned with the attacker and there is no impact.
- (3) If another bubble is filled in by the voter in the same race, the tabulator should report an *overvote*. The ballot is returned to the voter. The voter then decides whether to submit their ballot anyways or ask for a new ballot to be completed. In an attack by Bernherd et al. [63] voters do “not know what to do if they noticed a problem with their paper ballot during a real election.” In our experience, voters often resubmit their ballots.

What attack success rate can flip an election? In conventional adversarial machine learning, a high robust accuracy (low attack success rate) generally indicates an acceptable defense. For example, one of the most recent state-of-the-art defenses proposed in [64] achieved a robust accuracy of 70.69% against white-box adversarial machine learning attacks for the CIFAR-10 dataset. This robustness would correspond to a 29.31% attack success rate. Elections are routinely decided by small margins (Table 2). An attacker can reuse examples globally, though their reused examples would be subject to scanning noise discussed in Section 2.

We now illustrate how a small attack success rate can impact a close election. We consider a race with a 2% margin where 12% of ballots are left blank (the rate for Nevada state legislative races in 2020). We assume a two candidate race. Without an attack, Win will receive .415 fraction of the vote and Lose will receive .395 fraction of the vote. The adversary’s goal is for Lose to win over Win by a margin of .5% (often results under this margin trigger a hand recount). There are three relevant parameters:

- (1) What fraction of ballots carry an adversarial example for the Lose candidate? We call this parameter *deploy*.
- (2) What fraction of blank ballots with an adversarial example are misclassified? We denote this as *success*.

- (3) If the ballot has an adversarial example that is misclassified as a vote for Lose and the voter filled in a vote for Win their ballot will be marked as an overvote. When this occurs what fraction of the time does the voter ask for a new ballot? We call this probability $1 - \text{recast}$ and assume in this case the ballot is counted for Win. With probability *recast*, the voter asks the tabulator to accept the overvoted ballot and the ballot is not counted for either candidate.

Consider if the parameters are $\text{deploy} = 1$, $\text{success} = .1$, $\text{recast} = .3$, the votes for each candidate becomes

$$\text{Lose} := .395 + .12 \cdot \text{deploy} \cdot \text{success} = .407$$

$$\text{Win} := .415(1 - \text{deploy} \cdot \text{success} \cdot \text{recast}) = .407$$

Some blank ballots are converted to votes for Lose and some Win ballots are converted into overvotes which are not counted for either candidate. Looking ahead to Section 8, we achieve $\text{success} \approx .99$ on the most vulnerable model (a support vector machine); tested model’s vulnerability against realistic attacks varies widely (for more resilient models, $\text{success} = 0$ for imperceptible examples).

In the case when a voter refills their ballot after their ballot is marked as an overvote, the second ballot obtained by the voter may also contain an adversarial example that is misclassified as a vote. The overall fraction of ballots where this occurs for the parameters discussed is .13% of ballots. Continuing to use Nevada as an example, in 2020 the average state legislative race had 34K cast votes, so .13% of ballots corresponds to 43 ballots. Widespread occurrences of a voter having to request a new ballot multiple times is likely to arouse suspicion. This creates an incentive for the attack for $\text{deploy} \cdot \text{success}$ to be less than 1.

In summary, our analysis of attack success rate for the voting domain reveals a very important issue. In traditional adversarial machine learning a defense is successful if robust accuracy is 70%. As the example above shows, one can change the tabulated margin of a race by 2.5% even with a robust accuracy of 90%.

4.3 Generating Adversarial Examples

Adversarial examples can be created from clean images for a given model either through white-box or black-box adversarial attack methods [65, 66]. In both, an attacker begins with a clean unperturbed image and injects noise. Throughout this work, all clean images used to create adversarial examples are from the *Bubbles* datasets, we *never use a swatch image as a starting point*. This work focuses on white-box attacks due to VVSG 2.0 requirement 1.1.6G, which tabulators describe methods for classifying marks.

The most common method [65] to create adversarial images adds noise based on gradient information from the model. This is referred to as a white-box attack [67]. In this formulation, the gradient of the input with respect to a certain loss function is computed directly using the target model’s architecture and trained weight parameters. This attack is an optimization problem:

$$\max_{x_{adv}} \mathcal{L}(x_{adv}, y; \theta) \text{ subject to } \|x - x_{adv}\|_p \leq \epsilon \quad (1)$$

where \mathcal{L} is a loss function, x is a clean (non-perturbed) image with true class label y , θ represents the parameters of the model being attacked, ϵ is a bound on the magnitude of the perturbation and

$\|\cdot\|_p$ represents the l_p norm. The adversarial example is constrained to be at a distance at most ϵ from the original clean example.

We use the l_p norm with $p = \infty$ in our attacks. This is a widely used norm in adversarial machine learning [67–69]. We focus on APGD [12] but some of gradient masking results in the next section use PGD [13]. APGD is a SOTA white-box attack [64, 68, 69].

5 GRADIENT MASKING

Gradient masking frequently occurs in adversarial machine learning when evaluating the robustness of defenses to white-box attacks [65, 70]. Gradient masking is when the gradient of a model is incorrectly estimated in a white-box attack. This phenomena leads to the model having a falsely high robustness. Often, defenses are proposed and tested with attacks like FGSM and PGD, and are later broken by adaptive attacks which overcome gradient masking [15, 26, 66]. Gradient masking does not make a model secure.

For voting datasets, zero gradients occur when backpropagating the gradient in the SimpleCNN and ResNet-20 models during the attack. In addition, we observe non-monotonic behavior of APGD with increasing ϵ on VGG-16. It is important to note this occurs after the models have been trained. The models often exhibit maximal predictive confidence of either $[1, 0]$ or $[0, 1]$. In this section, we explore the extent of the issue and show that it is rooted in the numerical instability of floating point and datatypes used by PyTorch with NVIDIA GPUs. Furthermore, in Section 6, we show how a modified DLR loss can overcome this issue [12].

5.1 The Repeated Zero Gradient Condition

We demonstrate the occurrence of zero gradients in multiple different models trained on the voting datasets when conducting standard white-box adversarial attacks.

Experimental Setup. We attack three models (SVM, SimpleCNN, ResNet-20) trained on the grayscale datasets (*Gray-C* and *Gray-B*) using PGD. We set PGD to run for 20 steps using $\epsilon = 0.031$ with step size 0.00155. We randomly select 500 marks and 500 non-marks from the *Bubbles* validation set (no swatches) and 500 marks and 500 non-marks from the *Swatches only* (no bubbles) validation set that were correctly classified. At each of the k steps of PGD we check the maximum element of the absolute value of the gradient matrix. If $\max_i \left\{ \left| \partial L / \partial x_i^{(k)} \right| \right\} = 0.0$ then this step of PGD exhibits a zero gradient.

Analysis of Zero Gradient. The number of recorded instances of zero gradient across 20 steps are reported in Table 3. All 500 marks encounter a zero gradient for the first step on the SimpleCNN. All 500 marks and 500 non-marks encounter a zero gradient for the first step on ResNet-20. No example for the SVM encounters a zero gradient in the bubbles validation set. Note that while fewer swatch examples express a zero-gradient, only bubbles are considered a valid starting point for our attacks.

Analysis of Confidence. Our models return a tuple for their confidence in each class, vote then non-vote respectively. We provide the average confidence tuple (rounded to four decimal places) over each step for each class. Most notably, for classes and models that encounter a zero gradient for all 500 examples, the confidence is either $[1.0, 0.0]$ for votes or $[0.0, 1.0]$ for non-votes. Since each model

uses a softmax activation layer to normalize their outputs, a 1.0 is the maximum possible confidence for a class.

5.2 Numerical Instability

We devise an experiment that attributes zero-gradient to numerical instability arising from 32-bit floating point arithmetic as well as tensor-float arithmetic in use within the PyTorch implementation. We first introduce some notation on our target models.

Confidence and Gradient. A machine learning classifier receives an image as input x , forward propagates it through multiple layers $L_i(x) \rightarrow L_{i+1}(x)$, then outputs a confidence vector at the final layer. This output is the prediction this image belongs to each class \tilde{y} . The loss function \mathcal{L} derives how far the prediction \tilde{y} is from ground truth label y .

White-box adversarial machine learning attacks use gradient descent on the loss \mathcal{L} with respect to the source image⁸ x , i.e., $\frac{\partial \mathcal{L}}{\partial x}$, the gradient at the network input. A zero gradient $\frac{\partial \mathcal{L}}{\partial h} = 0$ appearing at some layer during the backpropagation will spread to shallower layer and induce 0 gradients all the way to the input layer, that is, all the way to $\frac{\partial \mathcal{L}}{\partial x}$. We observed zero gradient at the final softmax layer. We next review the specifics about floating point arithmetic to help understand the root cause.

Floating point refresher. IEEE-754 is the standard defining 32-bit floating point numbers. The use of fixed precision (32-bits $b_{31}b_{30} \cdots b_1b_0$), implies only certain numbers are representable. The standard calls for 1 bit for the sign b_{31} , 8 bits for the exponent $b_{30} \cdots b_{23}$ (using a bias representation) and 23 bits for the mantissa $b_{22} \cdots b_0$ to encode a *normal* floating point value:

$$(-1)^{b_{31}} \cdot 2^{(\sum_{i=23}^{30} b_i \cdot 2^{i-23}) - 127} \cdot \left(1 + \sum_{i=1}^{23} b_{23-i} \cdot 2^{-i} \right)$$

This representation uses an implicit 1 at the start of the mantissa. The smallest normal floating point is

$$(-1)^0 \cdot 2^{-126} \cdot (1 + 0) = 2^{-126} \approx 1.1754943508 \cdot 10^{-38}.$$

The range of representable floats can be *extended with de-normalized representations* where the first mantissa bit is zero. This broadens the range by using 0 bits at the most-significant end of the mantissa to boost the exponent at the expense of the number of digits of accuracy. The smallest de-normalized 32-bit floating point is $1.401298 \cdot 10^{-45}$ which, in binary, is all zeroes except the least significant bit of the mantissa. To retain accuracy, computed values should never drop past the smallest *normal* floating point.

PyTorch Floating Points. The most popular ML framework PyTorch uses the TensorFloat-32 (TF32 representation for floating point numbers supported by the NVIDIA hardware to compute convolutions).

This shorter representation uses only 10 bits of mantissa, 8 bits of exponents and a sign bit. They are designed *for speed* (about an order of magnitude faster) and are considered *good enough* for the precision expected by machine learning. The flags are, respectively, `torch.backends.cuda.matmul.allow_tf32` to enable them for matrix multiplications and `torch.backends.cudnn.allow_tf32` to enable them for convolutions. They were introduced in PyTorch

⁸This differs from gradient descent during training that computes the derivative with respect to network weights.

Training Dataset	Model	Class	Bubbles Validation Set		Swatches Validation Set	
			1st Step 0 Grad	Average Conf.	1st Step 0 Grad	Average Conf.
Gray-B	SVM	Mark	0	[0.9939, 0.0061]	0	[0.2871, 0.1408]
		Non-Mark	0	[0.1274, 0.8737]	0	[0.1512, 0.8488]
	SimpleCNN	Mark	500	[1.0, 0.0]	28	[0.8166, 0.0152]
		N-Mark	0	[1.3808e-21, 1.0]	0	[7.009e-21, 1.0]
	ResNet-20	Mark	500	[1.0, 0.0]	496	[0.9819, 2.2076e-6]
		N-Mark	500	[0.0, 1.0]	500	[0.0, 1.0]
Gray-C	SVM	Mark	0	[1.0, 1.0989e-09]	0	[0.2985, 0.1097]
		N-Mark	0	[0.0977, 0.1466]	0	[0.0658, 0.1112]
	SimpleCNN	Mark	498	[1.0, 2.4490e-29]	1	[0.4838, 0.0309]
		N-Mark	0	[0.0, 9.9425e-06]	0	[0.0258, 0.7107]
	ResNet-20	Mark	23	[0.2847, 0.0036]	304	[0.5023, 0.0007]
		N-Mark	156	[0.0020, 0.4903]	60	[0.0021, 0.2586]

Table 3: Zero Gradient Condition recorded over 20 steps of PGD. We record the number out of 500 of examples where zero gradient occurs on the first step, the average number of steps the zero gradient condition occurs in, and the confidence output out of 500 examples for each class.

version 1.7.⁹ By default, CNNs use TF32 for key computations during forward and backward passes.¹⁰

Manual Backpropagation. Models here contain a final linear layer that feeds into a softmax activation function. A linear layer accepts a feature vector h , performs matrix multiplication with weight matrix W , then adds a bias term b . The i^{th} column in the output z is the confidence the input image x belongs to $(i-1)^{th}$ class. The softmax layer exponentiates each column in z then normalizes them over their sum, returning the confidence vector \tilde{y} .

$$z = hW^T + b \rightarrow \tilde{y} = \frac{e^z}{\sum_{i=1}^C e^{z_i}}$$

This allows to evaluate the CE Loss. Note that y is the one-hot encoding of the image's class.

$$\mathcal{L} = - \sum_{i=1}^2 y_i \cdot \log(\tilde{y}_i)$$

Consider the gradient of this loss with respect to a feature vector h . We can express it w.r.t. the output of the linear layer z :

$$\frac{\partial \mathcal{L}}{\partial h} = \frac{\partial \mathcal{L}}{\partial z} \cdot \frac{\partial z}{\partial h}$$

Since $z = hW^T + b$, the derivative w.r.t. h is just the weight matrix $\frac{\partial z}{\partial h} = W^T$ and the derivative of the loss w.r.t. z is $\frac{\partial \mathcal{L}}{\partial z} = \tilde{y} - y$. The product of these terms delivers the full backpropagation equation.

Backpropagation Experiments. Both the accuracy of 32-bit floating point and the reduced accuracy of the TF-32 type contribute to zero gradients, indeed, the calculations of z and \tilde{y} involve convolutions in PyTorch.

32-bit Floating point accuracy. Consider two swatches A and B shown in Figure 2 that are members of the same class (their

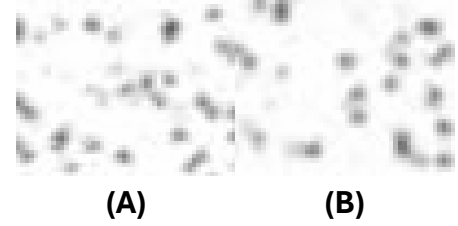


Figure 2: Examples of mark swatches considered for manual backpropagation. The ResNet-20 produces a zero gradient for Swatch (A) and a non-zero gradient for Swatch (B).

y vectors are $[1, 0]$). We chose mark swatches because of their visual similarity and they can exhibit zero gradients (see Table 3). Empirically, A triggers a zero-gradient while B does not. Given the fixed weights of the ResNet-20, we can manually compute z and \tilde{y} using the penultimate layer weights W and biases b . Namely:

$$z(A) = h(A) \cdot W^T + b, z(B) = h(B) \cdot W^T + b$$

as well as

$$\tilde{y}(A) = \frac{e^{z(A)}}{\sum_{i=1}^C e^{z_i(A)}}, \tilde{y}(B) = \frac{e^{z(B)}}{\sum_{i=1}^C e^{z_i(B)}}$$

Those values are used to compute $\frac{\partial \mathcal{L}}{\partial h} = (\tilde{y} - y) \cdot W$ for both A and B . To understand the stability issue, consider the following values for $z(A)$ and $z(B)$

$$z(A) = [49.218 \quad -48.582], z(B) = [18.516 \quad -18.059]$$

The last layer contains 2 neurons, so we get two z -values. Computing $\tilde{y}(A)$ produces

$$\begin{aligned} e^{z(A)} &= [e^{z_1(A)} \quad e^{z_2(A)}] = [e^{49.218} \quad e^{-48.582}] \\ &= [2.3720 \cdot 10^{21} \quad 7.9635 \cdot 10^{-22}] \end{aligned}$$

⁹PyTorch TF-32 <https://pytorch.org/docs/stable/notes/cuda.html#tf32-on-ampere>.

¹⁰There is no reason to expect this computation to match a sequential CPU computation as floating points are not commutative. GPUs will group operands differently and results may change.

To get $\tilde{y}(A)$, we compute $e^{z_1(A)} + e^{z_2(A)}$ as $2.3720 \cdot 10^{21}$, i.e., $e^{z_1(A)} + e^{z_2(A)} = e^{z_1(A)}$. The magnitude difference between $e^{z_1(A)}$ and $e^{z_2(A)}$ is so large that the second operand is *absorbed* by the first. The second ratio

$$\tilde{y}_2(A) = \frac{e^{z_2(A)}}{e^{z_1(A)} + e^{z_2(A)}} = 0$$

because the division of a very small number by a very large one underflows the float type. Overall, $\tilde{y}(A) = [1 \ 0]$ and the first factor of the gradient is $\tilde{y}(A) - y(A) = [1 \ 0] - [1 \ 0] = [0 \ 0]$. Interestingly, with B , the z values are a bit smaller leading to

$$e^{z(B)} = [1.1000 \cdot 10^8 \quad 1.4357 \cdot 10^{-8}]$$

and $\tilde{y}(B) = [9.999999 \cdot 10^{-1} \quad 1.305207 \cdot 10^{-16}]$ which does not trigger the zero gradient. The gradient expressions above were manually derived and evaluated with Octave [71] to independently confirm the observations. *With an FP32 representation, the back-propagation through the last layer can yields a zero gradient. Once this occurs, the preceding gradients will be 0 as well.*

TensorFloat 32-bit Floating point accuracy. Recall that PyTorch uses convolutions to compute z and \tilde{y} . Given the defaults used by PyTorch, these convolutions do rely on the numerically weaker TF32 type (10-bit mantissa). The accuracy of the z values and the \tilde{y} values are further reduced. This can increase the occurrence of zero gradients for the same reasons.

Since zero gradients are a direct consequence of the data types used within PyTorch for our datasets, we believe this phenomenon is likely to occur on bubble classifiers produced by industry and researchers. We note that while the problem could be made worse by the specialized datatypes with less precision on NVIDIA GPUs, the problem *still* occurs with classic 32-bit floating point. Turning off these datatypes has the undesirable effect of causing a $10\times$ slowdown during training. We have not tested behavior on models using 64-bit wide floating points.

One potential solution for the attacks is to employ a randomized start (commonly done in PGD and APGD). However, given that zero gradients are so frequent, they can *still* occur after the first step of the attack. In addition, randomized start does not provide a deterministic solution to the problem.

6 OVERCOMING THE ZERO GRADIENT CONDITION

The zero-gradient condition has previously been encountered [70] when assessing adversarial machine learning defenses. In our work gradient masking (zero gradients) occurs in the models trained on the ballot datasets, without any defenses implemented. To the best of our knowledge, we are the first to observe this phenomenon in classifiers without defensive mechanisms. We show how to overcome this issue using a modified version of the difference of logits ratio (DLR) function proposed in [12].

As an alternative to using cross-entropy (CE) loss, in [16] the Carlini and Wagner targeted attack was proposed in which the following loss function was minimized:

$$F(x) = \max(z(x)_t) - \max\{z(x)_j : j \neq t\} - \kappa \quad (2)$$

where $z(\cdot)_j$ is the j^{th} logit output from the model, $z(\cdot)_t$ represents the logit of the target class t and κ represents confidence with

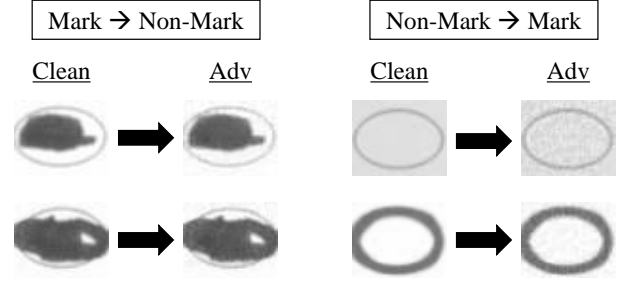


Figure 3: Examples of mark to non-mark and non-mark to mark adversarial attacks on the SimpleCNN. We abbreviate mark \rightarrow non-mark as *Under* and non-mark \rightarrow mark as *Over*. The examples above are created with APGD $\epsilon = 8/255$.

which the adversarial example should be misclassified. Further work in [12] proposed the use of DLR loss function:

$$\text{DLR}(x, y) = -\frac{z_y - \max_{j \neq y} z_j}{z_{\pi_1} - z_{\pi_3}} \quad (3)$$

where z_y is the logit output corresponding to the correct class label and π is a permutation that orders the elements of the logit output z in decreasing order. It is important to note that the DLR loss function is for multi-class classification where the number of classes C is greater than 3, since z_{π_3} is undefined for $C < 3$. However, the ballot datasets are binary classifications tasks ($C = 2$). Hence we modify the DLR loss function in Equation 3 by only using the numerator. Effectively this reduces DLR loss function to the untargeted version of the Carlini and Wagner loss function introduced in Equation 2, without the outer maximization and confidence κ . It is important to note that the denominator $z_{\pi_1} - z_{\pi_3}$ in Equation 3 was included for scale invariance to prevent gradient masking [12]. In our experiments, we observe that the binarized DLR loss operates as expected despite removing the denominator.

7 ADVERSARIAL ATTACKS IN THE VIRTUAL CONTEXT

The virtual context is a best-case scenario for an adversary. When crafting perturbations, we ignore artifacts (e.g., noise) introduced by the physical world. Performance in the more challenging *physical context* appears in Section 8.

Figure 3 shows how bubble images yield two different types of attacks. Recall that *Over* are adversarial marks that appear empty yet are classified as marks. Likewise, *Under* are adversarial mark that appear to be marks but are classified as blanks. Recall *Under* cannot be conducted by an attacker compromising a print vendor but are presented for completeness. The first set of experiments is designed to answer fundamental security questions:

- (1) Which attacks are most effective?
- (2) Does the *DLR* loss overcome the zero-gradient condition?
- (3) Does the training dataset impact model resilience?
- (4) Does model complexity impact attack success rate?
- (5) Do imperceptible ϵ alterations flip the classifier output?

7.1 White-Box Attack Performance

We first investigate the choice of attack. We use model robustness at each perturbation magnitude (ϵ value) to determine the best performing attack.

Experimental Setup. We attack six models (SVM, SimpleCNN, VGG-16, ResNet-20, CaiT, and Twins) trained on the grayscale datasets (*Gray-C* and *Gray-B*) using APGD. We consider two versions of APGD 1) with CE loss, 2) with DLR loss.

We randomly select 500 marks and 500 non-marks from the *Bubbles* validation set (no swatches) that were correctly classified by the target model. The choice of clean initial samples follows Mahmood, Mahmood, and van Dijk’s methodology [68]. For all attacks, ϵ varies from 4/255 to 255/255. We report the resulting robust accuracy in Table 4 for the *Gray-C* and *Gray-B* datasets.

Analysis of Attack Performance. Model robustness across all grayscale datasets are reported in Table 4. We additionally tested prior attacks of FGSM [72], MIM [14], and PGD [13]. In Appendix B, we show that all attacks on ResNet-20 using CE exhibit a non-zero robustness with $\epsilon = 255/255$ giving indication the zero-gradient condition occurs for all standard attacks (Table 10).

Training Dataset Matters. Usually, models trained on the *Gray-B* dataset deliver more robust accuracies than their counterparts trained on the *Gray-C* dataset. The only exception to this is the VGG-16 model which is much more robust when trained on *Gray-C*. The *Gray-B* SVM and SimpleCNN are completely robust up to $\epsilon = 32/255$, CaiT is completely robust until $\epsilon = 16/255$, and ResNet-20 is completely robust until $\epsilon = 8/255$.

The more challenging and realistic *Gray-C* training dataset conveys a different picture. Indeed, the SVM classifier accuracy drops to 50% with the smallest $\epsilon = 4/255$ while ResNet-20 and Twins drop much further, even for small values of ϵ . SimpleCNN and VGG-16 retain some resilience at small values of ϵ ($\leq 8/255$).

As expected, for the majority of the models, training on a more complex dataset that forces the classifier to learn marginal marks, thus moving the decision boundary in a way that makes adversarial attacks easier. The only exception to this rule is VGG-16 which we hypothesize is due to the VGG architecture. The literature has shown the VGG family of models to have other intriguing adversarial properties [73]. It is also worth noting that while VGG-16 trained on *Gray-C* is more robust than its bubbles counterpart, VGG-16 is not the most robust CNN model.

From a functionality standpoint though, tabulators must handle marginal marks. Recall from the Introduction and Table 1 that training on *Bubbles* reduces the clean accuracy of models tested on *Combined* by 12 – 15% drastically impacting the accuracy of the classifier on marginal marks. As a reminder, SVM actually increases performance on *Gray-C* by training on *Gray-B*, but is not accurate enough for practice when trained using either dataset. *One cannot sacrifice performance on marginal marks for resilience to adversarial examples.*

When compared to the first row of Table 4, all models trained on *RGB-C*, except ResNet-20, achieved similar or worse robustness than their *Gray-C* counterparts up to $\epsilon = 32/255$. We attribute this to more image channels creating a higher dimension space that is

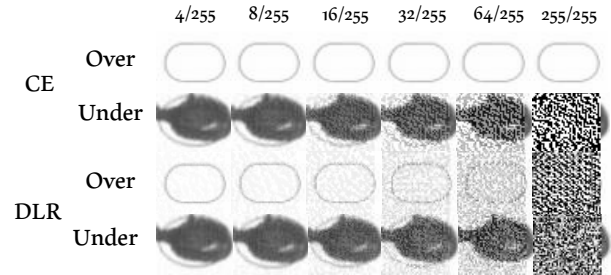


Figure 4: Adversarial examples from varying ϵ for APGD variants on ResNet-20 trained on *Gray-C* dataset. Note that the *Over* example in APGD-CE experiences gradient masking.

easier to exploit. As we discuss in Section 8, grayscale images are the preferred method in modern tabulation equipment.

Analysis of Model Complexity. Madry et al. argued that increasing model complexity increases robustness to single step adversarial machine learning attacks [13]. There does not seem to be a connection between model complexity and robust accuracy in our results. Tables 4 shows that Twins and ResNet-20 are the most vulnerable models while SimpleCNN and CaiT are the most resilient.

7.2 White-Box Perturbation Magnitude

We now investigate the choice of ϵ . A large ϵ yields noticeable adversarial perturbations. In conventional adversarial machine learning there is generally a monotonic relationship between robustness and ϵ i.e., increasing ϵ decreases robustness. However, for our datasets, CE APGD does not exhibit monotonic behavior for the CNN models as shown in Table 4. As discussed above, this is due to the difficulty in gradient estimation for these datasets. As an extreme example, VGG-16 on *Gray-C* with $\epsilon = 64/255$ has model robustness of 0 but $\epsilon = 255/255$ increases model robustness to .453. However, DLR APGD does exhibit monotonic behavior for all models.

Analysis of Attack Perturbation. Figure 4 shows attack images for varying ϵ when considering CE and DLR. The model under attack is ResNet-20 trained on *Gray-C*. We note the lack of increasing noise in the first row indicating gradient masking.

We now consider Figure 5 which shows increasing ϵ for each model using the DLR loss. For $\epsilon = 16/255$ the attack signal starts to be noticeable for all of our attacks. It is also worth noting that in Table 4, *Gray-C* SimpleCNN has robust accuracy of 0.5 at $\epsilon = 16/255$. At this point *Over* examples have all flipped class labels (without any changes of *Under* labels). Accuracy restricted to *Over* is shown in Table 5 as that is the focus of our physical world experiments. All six models have robustness of 0 for *Over* examples at $\epsilon = 16/255$. Attacks are easily detectable at the next noise level of $\epsilon = 32/255$. This noise level is when our attacks start creating *Under* examples for all models.

We consider attacks under 8/255 unnoticeable in the virtual domain and 16/255 unnoticeable in the physical domain, see Section 8.

Visibility of Examples Across Models. Figure 5 shows the impact of ϵ when attacking models trained on *Gray-C* using APGD. Only *Over* examples are shown since this represents the more successful

Model	Dataset	Loss	Clean Acc.	4/255	8/255	16/255	32/255	64/255	255/255
SVM	Gray-C	CE	.9171	.500	.500	.500	.499	0	0
	Gray-C	DLR		.500	.500	.500	.499	0	0
	Gray-B	CE	1.0000	1.000	1.000	1.000	1.000	.138	0
	Gray-B	DLR		1.000	1.000	1.000	1.000	.138	0
SimpleCNN	Gray-C	CE	1.0000	1.000	.825	.500	.498	.498	.500
	Gray-C	DLR		1.000	.824	.500	0	0	0
	Gray-B	CE	.9999	1.000	1.000	1.000	1.000	1.000	.500
	Gray-B	DLR		1.000	1.000	1.000	1.000	.584	0
VGG-16	Gray-C	CE	.9999	1.000	1.000	.492	.020	0	.453
	Gray-C	DLR		1.000	1.000	.495	.023	0	0
	Gray-B	CE	1.0000	.984	.134	0	0	0	0
	Gray-B	DLR		.984	.137	0	0	0	0
ResNet-20	Gray-C	CE	.9999	.168	.304	.647	.647	.645	.644
	Gray-C	DLR		0	0	0	0	0	0
	Gray-B	CE	.9998	1.000	1.000	1.000	1.000	1.000	1.000
	Gray-B	DLR		1.000	1.000	.995	.921	.500	0
CaiT	Gray-C	CE	.9995	1.000	1.000	.500	.499	.090	0
	Gray-C	DLR		1.000	1.000	.500	.499	.092	0
	Gray-B	CE	1.0000	1.000	1.000	1.000	.991	.501	0
	Gray-B	DLR		1.000	1.000	1.000	.991	.501	0
Twins	Gray-C	CE	1.0000	.243	0	0	0	0	0
	Gray-C	DLR		.011	0	0	0	0	0
	Gray-B	CE	1.0000	.979	.829	.303	0	0	0
	Gray-B	DLR		.979	.828	.282	0	0	0

Table 4: Robust Accuracy Results under APGD attack across models using CE and DLR losses on both *Gray-C* and *Gray-B* datasets.

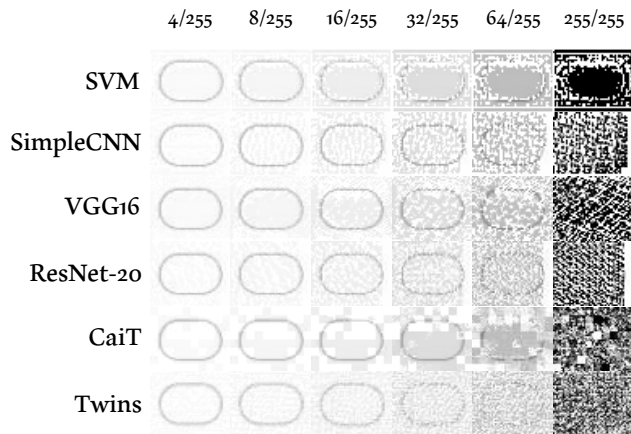


Figure 5: Adversarial examples from varying ϵ for APGD with DLR on models trained on *Gray-C* dataset.

attack setting in the physical domain. Figure 5 shows that for all models, $\epsilon \leq 8/255$ produces imperceptible perturbations. These perturbations become noticeable when $\epsilon \geq 16/255$. The amount of noise seems to qualitatively be the largest for the SVM and CaiT models. We also note attention artifacts appear clearly visible in attacks on the CaiT model. The noise level for the SimpleCNN, VGG-16, ResNet-20, and Twins models appears similar.

8 ATTACKS IN THE PHYSICAL WORLD

In this section, we consider the *Print* threat model in the physical world. This attack scenario uses an adversarial printer to generate *Over* examples on printed ballots. We start by reviewing prior work on physical world adversarial machine learning.

Prior Work. Wei et al. [74] surveyed adversarial machine learning in the physical world. Sharif et al. [75] designed targeted adversarial perturbations using a modified softmax loss function. They printed these 224×224 pixel images, of which approximately 6% area is covered by an adversarial patch in question that takes the shape of glasses. These adversarial glasses were then used to attack (evade) facial recognition systems. This work can be considered human-perceptible perturbations. Recall, that in our attacks, one must produce ballots that are indistinguishable from empty ballots. Kurakin, Goodfellow, and Bengio [76] use a modified version of FGSM to design untargeted perturbations at various degrees of ϵ and print clean and adversarial images, and classify using a phone camera. They use the CE loss function. These adversarial images are human imperceptible. Like our work, they also consider l_∞ distance. However, their work does not consider printer dithering that we now discuss.

Our Pipeline. We focus on *Over* examples that can be created by an adversarial printer. Attacks follow the following physical pipeline:

- (1) Adversarial example generation (see Section 7).
- (2) Layout on an empty page.
- (3) Printing using a commodity laserjet printer.
- (4) Scanning using a commodity scanner.

- (5) Image alignment, color correction, segmentation.
- (6) Classification using the target model.

Steps 2-5 are not needed in Section 7. This attack is not perfectly realistic in the following sense:

- (1) A ballot printer could use higher-end printing techniques (e.g., offset printing, or even photo-realistic printing) instead of laserjet printing.
- (2) We use ad hoc registration and segmentation. Yet, it appears to not introduce measurable/substantial error.

Vendors have moved away from *colored* ballots in favor of *black and white* ballots where colors are only decorative. This section further restricts the investigation to models trained on the *Combined* dataset to understand the impact of the physical world on models that could realistically serve in place of optical scanners.

8.1 Physical Dataset

All the models are trained as described in Section 3. However, physically extracted bubbles are first fed through a denoising autoencoder to remove the noise introduced in the printing process, then fed through a classifier. Without this denoiser, models had clean accuracy of under 90% on bubbles, see Table 8 in the Appendix. The denoiser is described in Appendix A.1. In comparison to previous physical attacks, we see substantial noise in classifying clean images when printing and scanning, due to 1) dithering of the printer and 2) printing a limited set of pixel values.

Layout. We layout all bubbles (40×50 at 200 dpi) in a matrix on a 8.5×11 inch sheet spread 0.5 inches apart. These sheets are printed and scanned. Registration corrects misalignment from the scanner, and extracts each bubble from their exact locations.

Printing. We used an HP LaserJet-3010 printer. It is a monochrome laser printer with max print speed of 42 pages per minute (ppm). It prints at 1200 dots per inch (dpi).

Scanner. The scanner is a Fujitsu-7600 with 24bpp and a standard automatic document feeder. We scanned in grayscale at 200 dpi. The software used is SANE. The dpi of the printer and scanner are multiples of each other (6x) to avoid fractional scaling.

Correction. We used Argyll with color calibration sheets (e.g., IT8) to tune the scanner with an ICC profile for color tonality errors.

The drop in accuracy. Printing and scanning, even with ICC correction techniques in place, introduces additional challenges. Images are visibly different from their digital source. LaserJet printers simulate gray by using dithering patterns to trick the human eye into seeing gray. The net result is that the printed (and re-scanned) bubbles are darker and noisier than the original material the models were trained on. As a result, the models classification accuracy drop from over 99% clean accuracy without printing to under 90%, see Table 8. To mitigate, we use a denoising autoencoder that we describe in Appendix A.1. Prepending this denoiser to our models makes them accurate at classifying images both before and after printing using the Laserjet printer.

8.2 Physical Attack Results

We run APGD with DLR loss for ϵ from $4/255$ to $255/255$ on all of our models. The examples are fed through the physical extraction

pipeline, the denoiser, then the classifier. We consider 500 non-mark bubbles pre-print and post-print. Our attacks only use the classifier weights. Future attacks could incorporate the denoiser weights as part of the backpropagation step.

Results are shown in Table 5. For $\epsilon = 16/255$ which we judge to be imperceptible in the physical domain, SVM and CaiT are very susceptible to post-print *Over* examples. ResNet-20 and Twins have some resilience but demonstrate robust accuracy less than 1.000. We note that ResNet-20 and Twins do not demonstrate monotonically decreasing robustness as ϵ increases. This non-monotonic behavior is unexpected, but our attacks are “unaware” of the print-scan noise. Interestingly, digital model robustness appears not to impact physical world resilience. The highly vulnerable digital models of VGG-16 and Twins are not especially vulnerable to our physical attacks. However, SVM is vulnerable in both domains.

Summary. Adversarial ML involving the physical world is more complicated with several sources of noise that can destroy adversarial signal such as dithering, scanning misalignment, and changes in intensity ranges. Nonetheless for the SVM, ResNet-20, Twins and CaiT *Over* attacks are viable. As a reminder, a printer can reuse a single attack image.

9 CONCLUSION

Prior work showed that BMDs can alter results and that not all voters check the printed ballot before tabulation [43, 44]. We show that a malicious or compromised ballot printing vendor can print ballots that will be misclassified, even if a voter inspects their ballots. While this work focuses on the l_∞ norm for adversarial samples, future work should consider other norms.

Since voting is not an area where one can sacrifice clean accuracy, four main recommendations emerge:

- (1) Transparency from vendors on mark interpretations,
- (2) Formalization of voter intent guidelines to allow for standardized labeled datasets with marginal marks,
- (3) Building mark models that mimic human perception, and
- (4) Explore user interfaces to privately alert voters whenever their ballot features marginal marks and catch risks of misinterpretation.

In summary, our work makes the following contributions:

- (1) We provide four new labeled ballot datasets to the security community.
- (2) We demonstrate that models trained on ballot data suffer from zero gradients, making standard white-box attacks unusable. We analyze this issue thoroughly and show the DLR loss allows APGD to be effective.
- (3) We show that for some models in the physical domain, scanning and printing adversarial examples yields an attack success rate high enough to flip the outcomes of elections with small margins where many voters leave the ballot blank.

ACKNOWLEDGMENTS

We thank the reviewers and Alexander Russell for their detailed comments and suggestions for improving this manuscript. This project was jointly funded by grants from the Connecticut Secretary of State’s Office and Department of Homeland Security on Grant

Model	Domain	Perturbation Magnitude						
		0/255	4/255	8/255	16/255	32/255	64/255	255/255
SVM	Digital	.874	0	0	0	0	0	0
	Phys.	.8480	.984	.226	0	0	0	0
SimpleCNN	Digital	1.000	1.000	.450	0	0	0	0
	Phys.	1.0000	1.000	1.000	1.000	1.000	1.000	0
VGG-16	Digital	1.0000	1.000	1.000	0	0	0	0
	Phys.	1.0000	1.000	1.000	1.000	1.000	.812	0
ResNet-20	Digital	1.000	0	0	0	0	0	0
	Phys.	0.9940	1.000	.984	.962	.996	.804	0
Twins	Digital	1.0000	.044	0	0	0	0	0
	Phys.	1.0000	.842	.842	.844	.842	.836	0
CaiT	Digital	1.0000	1.000	1.000	0	0	0	0
	Phys.	1.0000	1.000	.974	.136	0	0	0

Table 5: Model robustness against 500 pre/post-print *Over* and 500 pre-print examples generated using APGD with DLR loss. $\epsilon = 8/255$ is deemed imperceptible in the digital domain and $\epsilon = 16/255$ in the physical domain. Although *Over* is the only viable attack setting in the physical domain, model accuracy is much lower in the digital domain. We exclude the *Gray-B* dataset as physical attacks against these models were ineffective. The 0/255 column denotes the clean accuracy on 500 non-vote bubbles before printing and after the print and scan process.

Number #DHS-UNO 44-0108-1001-502. L. Michel was partially supported through the Synchrony Endowed Chair. B. Fuller was additionally supported through NSF grants #2141033 and 2232813.

REFERENCES

- [1] Ronald L Rivest and Philip B Stark. When is an election verifiable? 2017.
- [2] Sameer Barretto, William Chown, David Meyer, Aditya Soni, Atreya Tata, and J. Alex Halderman. Improving the accuracy of ballot scanners using supervised learning. In *Electronic Voting: 6th International Joint Conference, E-Vote-ID 2021, Virtual Event, October 5–8, 2021, Proceedings*, page 17–32, Berlin, Heidelberg, 2021. Springer-Verlag.
- [3] Ian J Goodfellow, Jonathon Shlens, and Christian Szegedy. Explaining and harnessing adversarial examples. *arXiv preprint arXiv:1412.6572*, 2014.
- [4] Christian Szegedy, Wojciech Zaremba, Ilya Sutskever, Joan Bruna, Dumitru Erhan, Ian Goodfellow, and Rob Fergus. Intriguing properties of neural networks. *arXiv preprint arXiv:1312.6199*, 2013.
- [5] Patrick McDaniel, Nicolas Papernot, and Z Berkay Celik. Machine learning in adversarial settings. *IEEE Security & Privacy*, 14(3):68–72, 2016.
- [6] Alexey Kurakin, Ian J Goodfellow, and Samy Bengio. Adversarial examples in the physical world. In *Artificial intelligence safety and security*, pages 99–112. Chapman and Hall/CRC, 2018.
- [7] Karen Simonyan and Andrew Zisserman. Very deep convolutional networks for large-scale image recognition. *arXiv preprint arXiv:1409.1556*, 2014.
- [8] Kaiming He, Xiangyu Zhang, Shaoqing Ren, and Jian Sun. Deep residual learning for image recognition. In *Proceedings of the IEEE conference on computer vision and pattern recognition*, pages 770–778, 2016.
- [9] Hugo Touvron, Matthieu Cord, Alexandre Sablayrolles, Gabriel Synnaeve, and Hervé Jégou. Going deeper with image transformers. In *Proceedings of the IEEE/CVF international conference on computer vision*, pages 32–42, 2021.
- [10] Xiangxiang Chu, Zhi Tian, Yuqing Wang, Bo Zhang, Haibing Ren, Xiaolin Wei, Huaxia Xia, and Chunhua Shen. Twins: Revisiting the design of spatial attention in vision transformers. *Advances in Neural Information Processing Systems*, 34:9355–9366, 2021.
- [11] UConn Voter Center. Uconn voter center - voting bubbles with swatches, May 2025. Available at <https://doi.org/10.5281/zenodo.15458710>.
- [12] Francesco Croce and Matthias Hein. Reliable evaluation of adversarial robustness with an ensemble of diverse parameter-free attacks. In *International conference on machine learning*, pages 2206–2216. PMLR, 2020.
- [13] Aleksander Madry, Aleksandar Makelov, Ludwig Schmidt, Dimitris Tsipras, and Adrian Vladu. Towards deep learning models resistant to adversarial attacks. In *International Conference on Learning Representations*, 2018.
- [14] Yinpeng Dong, Fangzhou Liao, Tianyu Pang, Hang Su, Jun Zhu, Xiaolin Hu, and Jianguo Li. Boosting adversarial attacks with momentum. In *Proceedings of the IEEE conference on computer vision and pattern recognition*, pages 9185–9193, 2018.
- [15] Nicholas Carlini and David Wagner. Adversarial examples are not easily detected: Bypassing ten detection methods. In *Proceedings of the 10th ACM workshop on artificial intelligence and security*, pages 3–14, 2017.
- [16] Nicholas Carlini and David Wagner. Towards evaluating the robustness of neural networks. In *2017 IEEE Symposium on Security and Privacy (SP)*, pages 39–57. Ieee, 2017.
- [17] Michael A Specter, James Koppel, and Daniel Weitzner. The ballot is busted before the blockchain: A security analysis of voatz, the first internet voting application used in {US}. federal elections. In *29th USENIX Security Symposium (USENIX Security 20)*, pages 1535–1553, 2020.
- [18] Josh Daniel Cohen Benaloh. *Verifiable secret-ballot elections*. Yale University, 1987.
- [19] Ben Adida. Helios: Web-based open-audit voting. In *USENIX security symposium*, volume 17, pages 335–348, 2008.
- [20] Josh Benaloh, Michael Naehrig, Olivier Pereira, and Dan S Wallach. Electionguard: a cryptographic toolkit to enable verifiable elections. In *USENIX Security*, 2024.
- [21] National Academies of Sciences Engineering and Medicine. *Securing the Vote: Protecting American Democracy*. National Academies Press, 2018.
- [22] Chiman Kwan, Bryan Chou, Li-Yun Martin Kwan, and Bence Budavari. Debayering rgbw color filter arrays: A pansharpening approach. In *2017 IEEE 8th Annual Ubiquitous Computing, Electronics and Mobile Communication Conference (UEMCON)*, pages 94–100. IEEE, 2017.
- [23] Tadayoshi Kohno, Adam Stubblefield, Aviel D Rubin, and Dan S Wallach. Analysis of an electronic voting system. In *IEEE Symposium on Security and Privacy, 2004. Proceedings, 2004*, pages 27–40. IEEE, 2004.
- [24] Harri Hursti. *The Black Box Report Security Alert: July 4, 2005 Critical Security Issues with Diebold Optical Scan Design*. Black Box Voting, 2005.
- [25] David Wagner, David Jefferson, Matt Bishop, Chris Karlof, and Naveen Sastry. Security analysis of the diebold accubasic interpreter. Technical report, 2006.
- [26] Tigran Antonyan, Seda Davtyan, Sotirios Kentros, Aggelos Kiayias, Laurent Michel, Nicolas Nicolaou, Alexander Russell, and Alexander A. Shvartsman. State-wide elections, optical scan voting systems, and the pursuit of integrity. *IEEE Transactions on Information Forensics and Security*, 4(4):597–610, 2009.
- [27] Russell J Jancewicz, Aggelos Kiayias, Laurent D Michel, Alexander C Russell, and Alexander A Shvartsman. Malicious takeover of voting systems: arbitrary code execution on optical scan voting terminals. In *Proceedings of the 28th Annual ACM Symposium on Applied Computing*, pages 1816–1823, 2013.
- [28] Seda Davtyan, Sotiris Kentros, Aggelos Kiayias, Laurent Michel, Nicolas Nicolaou, Alexander Russell, Andrew See, Narasimha Shashidhar, and Alexander A Shvartsman. Pre-election testing and post-election audit of optical scan voting terminal memory cards. In *EVT*, 2008.
- [29] Seda Davtyan, Sotiris Kentros, Aggelos Kiayias, Laurent Michel, Nicolas Nicolaou, Alexander Russell, Andrew See, Narasimha Shashidhar, and Alexander A Shvartsman. Taking total control of voting systems: Firmware manipulations on an optical scan voting terminal. In *Proceedings of the 2009 ACM symposium on Applied Computing*, pages 2049–2053, 2009.
- [30] Stephen Checkoway, Ariel J Feldman, Brian Kantor, J Alex Halderman, Edward W Felten, and Hovav Shacham. Can dres provide long-lasting security? the case of return-oriented programming and the avc advantage. *EVT/WOTE*, 2009, 2009.
- [31] Tigran Antonyan, Nicolas Nicolaou, Alexander A Shvartsman, and Therese Smith. Determining the causes of { AccuVote } optical scan voting terminal memory card

- failures. In *2010 Electronic Voting Technology Workshop/Workshop on Trustworthy Elections (EVT/WOTE 10)*, 2010.
- [32] Duncan A Buell, Eleanor Hare, Frank Heindel, Chip Moore, and Barbara Zia. Auditing a {DRE-Based} election in south carolina. In *2011 Electronic Voting Technology Workshop/Workshop on Trustworthy Elections (EVT/WOTE 11)*, 2011.
- [33] Mark Lindeman and Philip B Stark. A gentle introduction to risk-limiting audits. *IEEE Security & Privacy*, 10(5):42–49, 2012.
- [34] Filip Zagórski, Grant McClearn, Sarah Morin, Neal McBurnett, and Poorvi L Vora. Minerva—an efficient risk-limiting ballot polling audit. In *30th USENIX Security Symposium (USENIX Security 21)*, pages 3059–3076. USENIX Association, 2021.
- [35] Oliver Broadrick, Sarah Morin, Grant McClearn, Neal McBurnett, Poorvi L Vora, and Filip Zagórski. Simulations of ballot polling risk-limiting audits. In *International Conference on Financial Cryptography and Data Security*, pages 351–365. Springer, 2022.
- [36] Abigail Harrison, Benjamin Fuller, and Alexander Russell. Adaptive risk-limiting ballot comparison audits. In *IEEE Security & Privacy*, 2023.
- [37] Benjamin Fuller, Rashmi Pai, and Alexander Russell. The decisive power of indecision: Low-variance risk-limiting audits and election contestation via marginal mark recording. In *USENIX Security*, 2024.
- [38] J Alex Halderman. Analysis of the antrim county, michigan november 2020 election incident, 2021.
- [39] Election Assistance Commission. Voluntary voting system guidelines, 2005.
- [40] Clifford Tatum. The abc and 123s of the voluntary voting system guidelines. *Scitech Lawyer*, 14(3):28–30, 2018.
- [41] Whitney Quesenberry and Sharon J Laskowski. Handbook for vvsg 2.0 usability and accessibility test strategies. 2023.
- [42] Matthew Bernhard, Josh Benaloh, J Alex Halderman, Ronald L Rivest, Peter YA Ryan, Philip B Stark, Vanessa Teague, Poorvi L Vora, and Dan S Wallach. Public evidence from secret ballots. In *Electronic Voting: Second International Joint Conference, E-Vote-ID 2017, Bregenz, Austria, October 24-27, 2017, Proceedings 2*, pages 84–109. Springer, 2017.
- [43] Matthew Bernhard, Kartikeya Kandula, Jeremy Wink, and J Alex Halderman. Unclearballot: Automated ballot image manipulation. In *Electronic Voting: 4th International Joint Conference, E-Vote-ID 2019, Bregenz, Austria, October 1–4, 2019, Proceedings 4*, pages 14–31. Springer, 2019.
- [44] Matthew Bernhard, Allison McDonald, Henry Meng, Jensen Hwa, Nakul Bajaj, Kevin Chang, and J Alex Halderman. Can voters detect malicious manipulation of ballot marking devices? In *2020 IEEE Symposium on Security and Privacy (SP)*, pages 679–694. IEEE, 2020.
- [45] Braden L Crimmins, Dhanya Y Narayanan, Drew Springall, and J Alex Halderman. DVSorter: Ballot randomization flaws threaten voter privacy. In *33rd USENIX Security Symposium (USENIX Security 24)*, 2024.
- [46] Andrea Bajcsy, Ya-Shian Li-Baboud, Mary Brady, et al. Systematic measurement of marginal mark types on voting ballots, 2015. <https://nvlpubs.nist.gov/nistpubs/ir/2015/NIST.IR.8069.pdf>.
- [47] Corinna Cortes and Vladimir Vapnik. Support-vector networks. *Machine learning*, 20:273–297, 1995.
- [48] Bernhard E Boser, Isabelle M Guyon, and Vladimir N Vapnik. A training algorithm for optimal margin classifiers. In *Proceedings of the fifth annual workshop on Computational learning theory*, pages 144–152, 1992.
- [49] Nello Cristianini and John Shawe-Taylor. *An introduction to support vector machines and other kernel-based learning methods*. Cambridge university press, 2000.
- [50] André Elisseeff and Jason Weston. A kernel method for multi-labelled classification. *Advances in neural information processing systems*, 14, 2001.
- [51] Kaleel Mahmood, Pedro Latorre Carmona, Sina Shahbazmohamadi, Filiberto Pla, and Bahram Javidi. Real-time automated counterfeit integrated circuit detection using x-ray microscopy. *Applied Optics*, 54(13):D25–D32, 2015.
- [52] Yann LeCun, Bernhard Boser, John S Denker, Donnie Henderson, Richard E Howard, Wayne Hubbard, and Lawrence D Jackel. Backpropagation applied to handwritten zip code recognition. *Neural computation*, 1(4):541–551, 1989.
- [53] Alex Krizhevsky, Ilya Sutskever, and Geoffrey E Hinton. Imagenet classification with deep convolutional neural networks. *Advances in neural information processing systems*, 25, 2012.
- [54] Karen Simonyan. Very deep convolutional networks for large-scale image recognition. *arXiv preprint arXiv:1409.1556*, 2014.
- [55] Christian Szegedy, Wei Liu, Yangqing Jia, Pierre Sermanet, Scott Reed, Dragomir Anguelov, Dumitru Erhan, Vincent Vanhoucke, and Andrew Rabinovich. Going deeper with convolutions. In *Proceedings of the IEEE conference on computer vision and pattern recognition*, pages 1–9, 2015.
- [56] Christian Szegedy, Vincent Vanhoucke, Sergey Ioffe, Jon Shlens, and Zbigniew Wojna. Rethinking the inception architecture for computer vision. In *Proceedings of the IEEE conference on computer vision and pattern recognition*, pages 2818–2826, 2016.
- [57] Kaiming He and Jian Sun. Convolutional neural networks at constrained time cost. In *Proceedings of the IEEE conference on computer vision and pattern recognition*, pages 5353–5360, 2015.
- [58] Rupesh Kumar Srivastava, Klaus Greff, and Jürgen Schmidhuber. Highway networks. *arXiv preprint arXiv:1505.00387*, 2015.
- [59] Alexander Kolesnikov, Lucas Beyer, Xiaohua Zhai, Joan Puigcerver, Jessica Yung, Sylvain Gelly, and Neil Houlsby. Big transfer (bit): General visual representation learning. In *Computer Vision—ECCV 2020: 16th European Conference, Glasgow, UK, August 23–28, 2020, Proceedings, Part V 16*, pages 491–507. Springer, 2020.
- [60] Jingfeng Zhang, Xilie Xu, Bo Han, Gang Niu, Lizhen Cui, Masashi Sugiyama, and Mohan Kankanhalli. Attacks which do not kill training make adversarial learning stronger. In *International conference on machine learning*, pages 11278–11287. PMLR, 2020.
- [61] Kaleel Mahmood, Phuong Ha Nguyen, Lam M Nguyen, Thanh Nguyen, and Marten Van Dijk. Besting the black-box: barrier zones for adversarial example defense. *IEEE Access*, 10:1451–1474, 2021.
- [62] Alexey Dosovitskiy, Lucas Beyer, Alexander Kolesnikov, Dirk Weissenborn, Xi-aohua Zhai, Thomas Unterthiner, Mostafa Dehghani, Matthias Minderer, Georg Heigold, Sylvain Gelly, et al. An image is worth 16x16 words: Transformers for image recognition at scale. In *International Conference on Learning Representations*, 2020.
- [63] Matthew Bernhard. Risk-limiting audits: A practical systematization of knowledge. In *International Joint Conference on Electronic Voting*, 2021.
- [64] Zekai Wang, Tianyu Pang, Chao Du, Min Lin, Weiwei Liu, and Shuicheng Yan. Better diffusion models further improve adversarial training. In *International Conference on Machine Learning*, pages 36246–36263. PMLR, 2023.
- [65] Florian Tramer, Nicholas Carlini, Wieland Brendel, and Aleksander Madry. On adaptive attacks to adversarial example defenses. *Advances in neural information processing systems*, 33:1633–1645, 2020.
- [66] K Mahmood, D Gurevin, M van Dijk, and PH Nguyen. Beware the black-box: On the robustness of recent defenses to adversarial examples. *Entropy*, 23:1359, 2021.
- [67] Nicholas Carlini, Anish Athalye, Nicolas Papernot, Wieland Brendel, Jonas Rauber, Dimitris Tsipras, Ian Goodfellow, Aleksander Madry, and Alexey Kurakin. On evaluating adversarial robustness. *arXiv preprint arXiv:1902.06705*, 2019.
- [68] Kaleel Mahmood, Rigel Mahmood, and Marten Van Dijk. On the robustness of vision transformers to adversarial examples. In *Proceedings of the IEEE/CVF International Conference on Computer Vision*, pages 7838–7847, 2021.
- [69] Ethan Rathbun, Kaleel Mahmood, Sohaib Ahmad, Caiwen Ding, and Marten van Dijk. Game theoretic mixed experts for combinatorial adversarial machine learning. *arXiv preprint arXiv:2211.14669*, 2022.
- [70] Anish Athalye, Nicholas Carlini, and David Wagner. Obfuscated gradients give a false sense of security: Circumventing defenses to adversarial examples. In *International conference on machine learning*, pages 274–283. PMLR, 2018.
- [71] John W. Eaton, David Bateman, Søren Hauberg, and Rik Wehbring. *GNU Octave version 9.1.0 manual: a high-level interactive language for numerical computations*, 2024.
- [72] Ian Goodfellow, Jonathon Shlens, and Christian Szegedy. Explaining and harnessing adversarial examples. In *International Conference on Learning Representations*, 2015.
- [73] Dong Su, Huan Zhang, Hongge Chen, Jinfeng Yi, Pin-Yu Chen, and Yupeng Gao. Is robustness the cost of accuracy?—a comprehensive study on the robustness of 18 deep image classification models. In *Proceedings of the European conference on computer vision (ECCV)*, pages 631–648, 2018.
- [74] Hui Wei, Hao Tang, Xuemei Jia, Zhixiang Wang, Hanxun Yu, Zhuo Li, Shin’ichi Satoh, Luc Van Gool, and Zheng Wang. Physical adversarial attack meets computer vision: A decade survey. *IEEE Transactions on Pattern Analysis and Machine Intelligence*, 2024.
- [75] Mahmood Sharif, Sruti Bhagavatula, Lujo Bauer, and Michael K. Reiter. Accessorize to a crime: Real and stealthy attacks on state-of-the-art face recognition. In *Proceedings of the 2016 ACM SIGSAC Conference on Computer and Communications Security, CCS ’16*, page 1528–1540, New York, NY, USA, 2016. Association for Computing Machinery.
- [76] Alexey Kurakin, Ian J Goodfellow, and Samy Bengio. Adversarial examples in the physical world. In *Artificial intelligence safety and security*, pages 99–112. Chapman and Hall/CRC, 2018.
- [77] F. Pedregosa, G. Varoquaux, A. Gramfort, V. Michel, B. Thirion, O. Grisel, M. Blondel, P. Prettenhofer, R. Weiss, V. Dubourg, J. Vanderplas, A. Passos, D. Cournapeau, M. Brucher, M. Perrot, and E. Duchesnay. Scikit-learn: Machine learning in Python. *Journal of Machine Learning Research*, 12:2825–2830, 2011.

A FULL DESCRIPTION OF TRAINING MODELS

We discuss how our classifiers are trained.

Adjusting Training Loader. We have four datasets, Bubbles-Grayscale, Bubbles-RGB, Combined-Grayscale and Combined-RGB. All models are trained on grayscale with SVM, SimpleCNN, ResNet-20, and Twins also trained on RGB. We use an 80-20 training-validation split. All of these datasets have a disproportional high amount of non-mark examples compared to mark examples. We

Dataset	Model	Hyperparameters				
		LR	DR	Epochs	WD	BS
<i>Gray-B</i>	SimpleCNN	0.01	0.9	20	0.0	512
	VGG-16	0.001	-	20	-	64
	ResNet-20	0.1	0.9	20	0.0	64
<i>Gray-C</i>	SimpleCNN	0.001	0.9	100	0.0	256
	VGG-16	0.001	-	20	-	64
	ResNet-20	0.0005	0.5	300	0.0	128
<i>RGB-B</i>	SimpleCNN	0.01	0.9	20	0.0	512
	ResNet-20	0.1	0.9	20	0.0	64
<i>RGB-C</i>	SimpleCNN	0.001	0.9	100	0.0	512
	ResNet-20	0.0005	0.5	300	0.0	128

Table 6: Training hyperparameters for convolutional models SimpleCNN and ResNet-20 across all four datasets. Abbreviations stand for Learning Rate, Dropout Rate, Epochs, Weight Decay, and Batch Size respectively.

balance our training loader to have an equal amount of mark and non-mark examples.

Training SVM. SVMs are linear classifier which maximize the distance between the decision boundary and each class in the latent space. They are much simpler than other models. We trained linear SVMs, meaning the linear, or “identity”, kernel was used. For grayscale datasets, examples were flattened from image size $1 \times 40 \times 50$ to a 2000 element tensor as the SVM’s input. Likewise, for color datasets, examples were flattened from $3 \times 40 \times 50$ to 6000. To match these input dimensions, grayscale SVMs consisted of a single fully-connected layer with 2000 input neurons to a single output neuron. Color SVMs had 6000 input neurons.

All SVM models were trained using the LinearSVC module from sklearn [77] with the same hyperparameters. We use a linear kernel with ℓ_2 penalty and balanced class weight. We use a regularization parameter of $1e - 8$, a tolerance of $1e - 7$, and an intercept scaling factor of 1000. We use primal instead of dual optimization and set the random state to 0.

Training CNNs. Training hyperparameters for the SimpleCNN, VGG-16, and ResNet-20 are listed in Table 6. Models are trained using CE loss and an Adam optimizer. VGG-16 was not trained on the color datasets.

Table 7 outlines the architecture layer-by-layer for the shallow convolutional neural network SimpleCNN. The entire model consists of three convolutional layers that send a one or three channel input (for grayscale and RGB respectively) to 32, to 48, then to 32 channels. The SimpleCNN use in-place ReLU operations with convolution, max pooling, or transposed convolution layer have a padding of 0. (We do the same on the denoiser.)

Training CaiT. We train the *Gray-B* and *Gray-C* datasets on CaiT from scratch. The same set of hyperparameters was used for training each dataset for 20 epochs each. Other hyperparameters include: patch size of 5, embedding dimension of 512, 16 transformer layers, 8 attention heads, MLP dimension of 2048, and dropout and embedding dropout rates of 0.1, along with a layer dropout of 0.05. The models are trained using CE loss and Adam optimizer with learning rate of $5e-5$ and batch size of 128.

Training Twins. The Twins-B model was originally pre-trained on ImageNet with RGB images of size 224×224 . We leveraged this pre-training to more quickly fine-tune the models trained on the *RGB-C* and *RGB-B* datasets. Transfer learning is not possible for the *Gray-C* and *Gray-B* datasets, however, as grayscale images only have one channel. Thus, these models were trained from scratch.

Twins was trained with the same set of hyperparameters for each dataset. Each Twins model was trained for 300 epochs with a batch size of 64. All images were upsampled to a resolution of 224×224 during training, evaluation, and attacks. We use an AdamW optimizer with an epsilon of $1e - 8$, no beta term, gradient norm clip of 5, a momentum term of 0.9, and a weight decay of 0.05. Dropout was not used during training or evaluation.

Additional Adjustments. We list some important optimizations used here:

- (1) We trained our self-attention model, the Twins, on a data range of 0-255 whereas our CNNs (SimpleCNN, VGG-16, and ResNet-20) and linear model, the SVM, were trained on a data range of 0-1. This is because the original Twins model, trained on ImageNet, was trained using a 0-255 range. This allowed us to transfer the model’s weights from ImageNet to the *RGB-C* and *RGB-B* datasets.
- (2) Adding a dropout layer before the final fully-connected layers of each convolutional model and using a high dropout rate helped our combined models achieve high validation accuracy.
- (3) Training on bubbles across all models was significantly easier than training on the combined dataset. Combined models required many epochs to reach a certain accuracy threshold, whereas bubble-only models required a few epochs to reach 100% training accuracy.
- (4) To perform CE attacks on the SVM, we add a two-node fully connected layer. The first neuron in our new output FC layer has a weight of -1 and a bias of 1, and the second neuron has a weight of 1 and a bias of 0. This ensures that if the output of our first FC layer is p , the output of our second FC layer is $[p, 1 - p]$.
- (5) Downsizing 224×224 images to 40×50 then upscaling back to 224×224 removes most of the adversarial signal added to the original images. We need to downsize 224×224 images from Twins for printing and scanning. We run attacks on 40×50 images using Twins by performing an upscaling transformation in Twins’ forward pass.

Results. Our fine tuning has allowed almost all of our models across all of our datasets to achieve a $> 99\%$ clean validation accuracy on the bubbles dataset for all models except the SVM. Similarly, except the SVM, all combined models achieve a combined validation accuracy above 90%.

A.1 Training Denoiser

We used 100 training epochs with a fixed learning rate of 0.001 and Mean Squared Error loss. To learn the mapping, we train on 10,000 pairs of examples of pre-print/post-print bubbles. We also include 10,000 digital/digital identity pairs in training to ensure

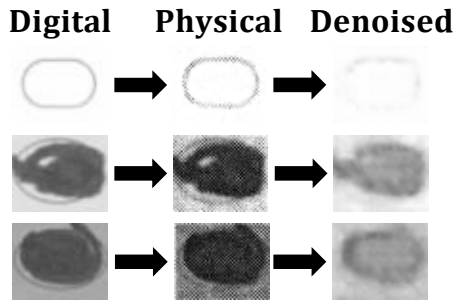


Figure 6: Comparison of examples in digital domain, physical domain, and denoiser output. To mitigate the darker tones and dithering in the physical domain, the denoiser adds a blurring effect.

Layer Type	Parameters
Input	(Num Channels, 40, 50)
Convolution + ReLU	32×3×3, stride 1
Max Pooling	2 × 2, stride 0
Convolution + ReLU	48 ×3×3, stride 1
Max Pooling	2 × 2, stride 0
Convolution + ReLU	32 ×3×3, stride 1
Max Pooling	2 × 2, stride 0
Dropout	0.5
FC + Softmax	2
Total Parameters	Grayscale: 28,818 RGB: 29,394

Table 7: SimpleCNN Architecture. Note the grayscale dataset has one input channel whereas the RGB dataset has three. This causes the total number of training parameters to vary.

	Sec. 3.2 Model		Post-Denoiser	
	Digital	Physical	Digital	Physical
SVM	0.937	0.806	0.913	0.924
SimpleCNN	1.000	0.750	1.000	1.000
ResNet-20	1.000	0.764	0.998	0.996
Twins	1.000	0.855	1.000	1.000

Table 8: Accuracy of all models trained on the *Gray-C* dataset on 1000 random classwise balanced *Gray-B* examples pre-print and post-print. Our models achieve a higher clean accuracy in the post print domain when using a denoiser.

	Layers	Parameters
	Encoder	Convolution + ReLU
Max Pooling		2 × 2, stride 0
Convolution + ReLU		16 × 3 × 3, stride 1
Max Pooling		2 × 2, stride 0
Convolution + ReLU		8 × 3 × 3, stride 1
Max Pool 3		2 × 2, stride 0
Decoder	Transpose + ReLU	8 × 3 × 3, pad 0, stride 2
	Transpose + ReLU	16 × 2 × 2, stride 2
	Transpose + ReLU	32 × 2 × 2, stride 2
	Transpose	1 × 3 × 3, stride 0

Table 9: Denoising Autoencoder Architecture. The images produced have dimension 42 × 50, the forward function removes the first and last row.

that the denoiser can handle images that have not been printed. No adversarial examples were involved in training.

Results are shown in Table 8, with the denoiser-augmented models demonstrating high 99% accuracy (on three of the models) when given printed or digital examples. SVM pre-print accuracy is lower with an accuracy of 91.3%. We print and scan 1000 random classwise balanced *Gray-B* examples.

Figure 6 illustrates how the denoiser reverses the darkening and dithering induced by printing. This carries a cost as images lose some *sharpness*. Denoiser-prepended models have high accuracy on both digital and physical samples. In the rest of this section, post-print adversarial examples are fed through the denoiser first before classification.

B ALTERNATIVE ATTACK RESULTS: PGD, MIM, FGSM

For ResNet-20, we believe gradient masking occurs on APGD [12], PGD [13], MIM [14], and FGSM [72]. Attack results using CE loss are shown in Table 10. We highlight a few results. First, as previously stated in the literature [67], unbounded attacks should always produce a robustness of 0%. This does *not* happen for any of the attacks with $\epsilon = 255/255$ (except FGSM on ResNet-20 Gray-B). **Every iterative attack (MIM, PGD and APGD) suffers from gradient masking when the CE loss function is used for ResNet-20.** For example, the MIM attack is 16% robust for $\epsilon = 255/255$ for ResNet-20 Gray-C when we would expect this number to be 0. Therefore when working to overcome gradient masking, we focused on refining the APGD attack. We choose to focus on APGD for the following two reasons. First, previous experimental findings [12, 68] showed that APGD offers superior attack performance in most cases when attacking CNNs and transformers. Second, the literature [67] clearly states using multiple iterative white-box attacks is not a useful form of analysis. Therefore, we did not further develop MIM, PGD and FGSM and instead focused on the APGD attack in our paper. We leave it as an open future work to see whether these attacks could be improved through alternative loss functions.

C ETHICAL CONSIDERATION

This paper addresses the susceptibility of machine learning models trained on voting bubbles to adversarial examples. To the best of our knowledge, **none of the models we have trained and attacked in this paper are used in real tabulating machines.** These models are also not chosen to be similar to models in use by vendors. Models were chosen to represent different possible design choices.

The marginal marks used in this dataset are designed to explore the boundary of an optical lens scanner and do not result from any election related data. The empty bubbles are bubbles that were printed by a commercial vendor. They have undergone registration and segmentation using predetermined coordinates. Marks are on paper printed by the same vendor. There are no obvious indications of the relevant election, ballot type, or what preferences were selected in the processed dataset.

Metric	APGD	PGD	MIM	FGSM
Dataset	<i>Gray-B/ Gray-C</i>	<i>Gray-B/ Gray-C</i>	<i>Gray-B/ Gray-C</i>	<i>Gray-B/ Gray-C</i>
Clean Acc.	0.9998 / 0.9999	0.9998 / 0.9999	0.9998 / 0.9999	0.9998 / 0.9999
4/255	1.000 / 0.168	1.000 / 0.166	1.000 / 0.166	1.000 / 0.721
8/255	1.000 / 0.304	1.000 / 0.166	1.000 / 0.166	1.000 / 0.751
16/255	1.000 / 0.647	1.000 / 0.166	1.000 / 0.166	0.995 / 0.668
32/255	1.000 / 0.647	1.000 / 0.166	1.000 / 0.166	0.924 / 0.652
64/255	1.000 / 0.645	1.000 / 0.166	1.000 / 0.166	0.500 / 0.642
255/255	1.000 / 0.644	1.000 / 0.166	1.000 / 0.166	0.000 / 0.480

Table 10: ResNet-20 Robust Accuracy on FGSM, PGD, MIM, and APGD, using Cross-Entropy loss.